LETTER

doi:10.1038/nature23005

Experimental signatures of the mixed axial–gravitational anomaly in the Weyl semimetal NbP

Johannes Gooth[1,2], Anna C. Niemann[1,3], Tobias Meng[4], Adolfo G. Grushin[5], Karl Landsteiner[6], Bernd Gotsmann[2], Fabian Menges[2], Marcus Schmidt[7], Chandra Shekhar[7], Vicky Süß[7], Ruben Hühne[3], Bernd Rellinghaus[3], Claudia Felser[7], Binghai Yan[7,8] & Kornelius Nielsch[1,3]

The conservation laws, such as those of charge, energy and momentum, have a central role in physics. In some special cases, classical conservation laws are broken at the quantum level by quantum fluctuations, in which case the theory is said to have quantum anomalies[1]. One of the most prominent examples is the chiral anomaly[2,3], which involves massless chiral fermions. These particles have their spin, or internal angular momentum, aligned either parallel or antiparallel with their linear momentum, labelled as left and right chirality, respectively. In three spatial dimensions, the chiral anomaly is the breakdown (as a result of externally applied parallel electric and magnetic fields[4]) of the classical conservation law that dictates that the number of massless fermions of each chirality are separately conserved. The current that measures the difference between left- and right-handed particles is called the axial current and is not conserved at the quantum level. In addition, an underlying curved space-time provides a distinct contribution to a chiral imbalance, an effect known as the mixed axial–gravitational anomaly[1], but this anomaly has yet to be confirmed experimentally. However, the presence of a mixed gauge–gravitational anomaly has recently been tied to thermoelectrical transport in a magnetic field[5,6], even in flat space-time, suggesting that such types of mixed anomaly could be experimentally probed in condensed matter systems known as Weyl semimetals[7]. Here, using a temperature gradient, we observe experimentally a positive magneto-thermoelectric conductance in the Weyl semimetal niobium phosphide (NbP) for collinear temperature gradients and magnetic fields that vanishes in the ultra-quantum limit, when only a single Landau level is occupied. This observation is consistent with the presence of a mixed axial–gravitational anomaly, providing clear evidence for a theoretical concept that has so far eluded experimental detection.

Weyl semimetals are materials in which electrons behave as a type of massless relativistic particle known as a Weyl fermion. Massless chiral fermions exist where conductance and valence bands in these materials touch in isolated points, so-called Weyl nodes. At energies near these points the electrons are effectively described by the Weyl Hamiltonian[8,9], which implies that the energy of these Weyl fermions scales linearly with their momentum. Weyl nodes occur in pairs of opposite chirality[10] that, in the absence of additional symmetries, are topologically stable when they are separated in momentum space (Fig. 1a). Chiral Weyl fermions are subject to a chiral anomaly, which results in a strong positive magneto-conductance that can be detected experimentally[4,11]. Inspired by the pioneering studies of the chiral anomaly in pion physics[2,3], several research groups have recently reported on the observation of chiral-anomaly-induced positive longitudinal magneto-conductance in Na_3Bi (ref. 12), TaAs (ref. 13), NbP (ref. 14), GdPtBi (ref. 15), Cd_2As_3 (ref. 16), TaP (ref. 17) and RPtBi (ref. 18). Three-dimensional chiral fermions are theoretically predicted to also exhibit a mixed axial–gravitational anomaly[19,20]. In curved space-time, this anomaly contributes to the violation of the covariant conservation laws of the axial current, which are relevant to the chiral anomaly, and to the conservation law for the energy–momentum tensor[21]. The energy–momentum tensor encodes the density and flux of energy and momentum of a system. The mixed axial–gravitational anomaly has been suggested to be relevant to the hydrodynamic description of neutron stars[22], and to the chiral vortical effect in the context of quark–gluon plasmas[5]. However, a clear experimental signature has yet to be reported.

Although the flatness of space-time would imply that gravitational anomalies are irrelevant for condensed matter systems, it has been recently understood that the presence or absence of a positive magneto-thermoelectric conductance for Weyl fermions is tied to the presence or absence of a mixed axial–gravitational anomaly in flat space-time[5,6]. The connection between the mixed axial–gravitational anomaly and the observed positive magneto-thermoelectric conductance can be understood by a calculation based on the conservation laws for charge and energy, and the standard Kubo formalism for the conductivities (Methods). Because the Weyl semimetal lives in a flat space-time, the mixed axial–gravitational anomaly does not affect the conservation laws for charge and energy directly. An anomalous contribution to the energy current has nevertheless been identified in the Kubo formalism[22]. Inserting this contribution into the conservation laws and using a simple approximation for the relaxation time, we find that thermoelectric transport in flat space-time is explicitly modified as a result of the presence of the mixed axial–gravitational anomaly in the underlying field theory.

The connection between thermal transport and the mixed axial–gravitational anomaly is also apparent in a relativistic quantum field theory computation of transport properties[5] and in the hydrodynamic formalism of the effective chiral electron liquid[6]. In the latter approach, the presence of a mixed axial–gravitational anomaly modifies the thermodynamic constitutive relations of the current and energy–momentum tensor in terms of gradients of the relevant hydrodynamic variables: temperature, chemical potential and velocity[6]. These modifications can be viewed as the hydrodynamic equivalent of the anomalous contributions to the energy current identified in the Kubo formalism. Although the Kubo-based calculation (Methods) is thus qualitatively consistent with the hydrodynamic calculation[6], transport in current Weyl semimetal samples is not consistent with the hydrodynamic regime, which involves strong interactions and features fast energy–momentum relaxation between the nodes. The predicted positive magneto-thermoelectric conductance is also consistent with

[1]Institute of Nanostructure and Solid State Physics, Universität Hamburg, Jungiusstraße 11, 20355 Hamburg, Germany. [2]IBM Research -Zurich, Säumerstrasse 4, 8803 Rüschlikon, Switzerland. [3]Leibniz Institute for Solid State and Materials Research Dresden, Institute for Metallic Materials, Helmholtzstraße 20, 01069 Dresden, Germany. [4]Institute for Theoretical Physics, Technical University Dresden, Zellescher Weg 17, 01062 Dresden, Germany. [5]Department of Physics, University of California, Berkeley, California 94720, USA. [6]Instituto de Física Teórica UAM/CSIC, Nicolás Cabrera 13–15, Universidad Autónoma de Madrid, Cantoblanco, 28049 Madrid, Spain. [7]Max Planck Institute for Chemical Physics of Solids, Nöthnitzer Straße 40, 01187 Dresden, Germany. [8]Department of Condensed Matter Physics, Weizmann Institute of Science, 7610001 Rehovot, Israel.

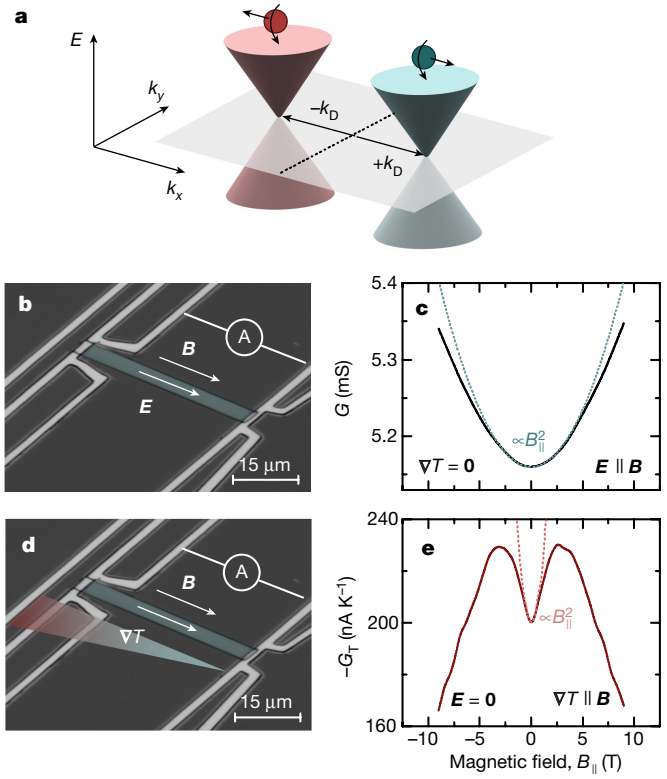

Figure 1 | Positive magneto-conductance $G(B_\parallel)$ and magneto-thermoelectric conductance $G_T(B_\parallel)$ in the Weyl semimetal NbP. **a**, Sketch of two Weyl cones with distinct chiralities $+\chi$ and $-\chi$, represented in green and red, respectively. E, k_x and k_y are the energy and the components of the momentum vector $\boldsymbol{k}$ in x and y directions, respectively. k_D denotes the distance of the chiral nodes from their centre point in momentum space. **b**, **c**, False-coloured optical micrographs of the devices used to measure the electrical conductance $G = J/E$ (**b**) and thermoelectric conductance $G_T = J/|\nabla T|$ (**c**). The red and the green ends of the colour gradient denote the hot and cold sides of the device, respectively. Four NbP micro-ribbons (green) were investigated, all showing similar results. The data for the first ribbon are presented here. **d**, **e**, $G(\boldsymbol{E} \parallel \boldsymbol{B})$ (**d**) and $-G_T(\nabla \boldsymbol{T} \parallel \boldsymbol{B})$ (**e**) as functions of the magnetic field $B_\parallel$ at a cryostat base temperature of $T = 25$ K (solid lines); the negative sign accounts for electron transport. The dotted lines show the predicted dependence ($\propto B_\parallel^2$).

the semi-classical approach based on the Boltzmann equation[23–26], which so far lacks a simple connection to the anomalous origin of this contribution. This consistency of different theoretical approaches illustrates that anomalies affect transport on a fundamental level; their effect can consistently be derived from any calculation that keeps track of conservation laws and symmetries, and that correctly captures the topological character of a Weyl node.

The positive magneto-conductance and magneto-thermoelectric conductance are fundamentally linked to the response of the charge current $\boldsymbol{J}$ when an electric field $\boldsymbol{E}$ and a thermal gradient ∇T are applied through the relation $\boldsymbol{J} = G\boldsymbol{E} + G_T \nabla T$. Here, $G = J/E$ denotes the electric conductance, which characterizes the response of the electrical current to electric fields, and $G_T = J/|\nabla T|$ is the thermoelectric conductance, which characterizes the electrical current in the Weyl metal that is induced by a temperature gradient. (Note that we define the coordinate system such that the applied temperature gradient has only one non-zero component.) In low magnetic fields, the mixed axial–gravitational anomaly and the chiral anomaly implies a positive magneto-current contribution to the transport coefficients $G = d_e + c_1 a_c^2 B_\parallel^2$ and $G_T = d_{th} + c_2 a_c a_g B_\parallel^2$, with $c_{1,2} > 0$ accounting for details of the band structure. Here d_e and d_{th} express the classical electrical and thermal Drude parts, the coefficients a_c and a_g account for the contributions of the chiral and mixed axial–gravitational anomalies, respectively[6,23,24,27], and $B_\parallel$ denotes the component of the magnetic field that is parallel to the electric field or thermal gradient. In the ultra-quantum limit at high magnetic fields, when only the lowest Landau level contributes to transport, G depends linearly on the magnetic field and the gravitational anomaly does not contribute to G_T (see Methods). Analogously to the positive magneto-conductance, which requires parallel electric and magnetic fields as determined by the chiral anomaly, the positive magneto-thermoelectric conductance is expected to be locked to the magnetic-field direction as a result of the anomalous contribution[6,23–26]. The combined measurement of (i) a finite value of a_g, (ii) the functional dependence for $\nabla T \cdot \boldsymbol{B} \neq 0$ of the positive magneto-thermoelectric conductance at low fields ($\boldsymbol{B}$ is the magnetic field), and (iii) the absence of positive magneto-thermoelectric conductance at high fields represents the experimental signature of the mixed axial–gravitational anomaly in thermal transport.

The magneto-thermoelectrical conductance of the half-Heusler alloy GdPtBi (ref. 15) has recently been calculated from separate measurements of thermopower and electrical conductance, revealing a positive magneto-thermoelectric conductance contribution at low magnetic fields. However, this contribution was interpreted as a signature of the node creation process, which depends on the magnetic field. To obtain experimental signatures of the presence of the mixed axial–gravitational anomaly, it is therefore desirable to go beyond these experiments and investigate the electrical response of intrinsic Weyl semimetals to temperature gradients in collinear magnetic fields.

For our experiments, we used micro-ribbons (50 μm × 2.5 μm × 0.5 μm) cut out from single-crystalline bulk samples of the Weyl semimetal NbP with a gallium focused-ion beam. The transport direction in our samples matches the [100] axis of the crystal (see Methods for details). An on-chip micro-strip line heater near the micro-ribbon generates a temperature gradient along the length of the ribbon, with the resulting temperature differences (less than 350 mK) sufficiently small to ensure that the measurement is in the linear response regime (Extended Data Fig. 6). The temperature gradient ∇T was measured by resistance thermometry using two metal four-probe thermometer lines located at the ends of the NbP micro-ribbon (Fig. 1d). The metal lines for thermometry also serve as electrodes for applying an electrical bias and for measuring the current response of the ribbon. The elongated geometry of the micro-ribbons, with contact lines across the full widths of the samples, was chosen to ensure that current jetting is suppressed and to provide homogenous field distributions[15,17]. To justify the description of the carriers in terms of Weyl fermions, it is essential that the Fermi level E_F is as close as possible to the Weyl nodes of NbP (refs 28, 29). By means of gallium doping, we recently showed that E_F is located only 5 meV above the Weyl points, in the electron cone of our NbP sample[14].

In a first set of transport experiments of electrical conductance measurements under isothermal conditions ($\nabla T = \boldsymbol{0}$), we establish that the NbP micro-ribbon can be accurately described by Weyl fermions. For this purpose, a voltage $V = 1$ mV is applied along the ribbon, which sets an electric field $\boldsymbol{E}$, and the corresponding current $\boldsymbol{J}$ is measured through a near-zero-impedance (1 Ω) ammeter. When the magnetic field is switched on, the Weyl nodes split into Landau levels. For each Weyl node, the zeroth Landau level disperses linearly with momentum along $\boldsymbol{B}$ (Fig. 2a) and is thus chiral, unlike the remaining Landau levels, which disperse quadratically. Aligned electric and magnetic fields ($\boldsymbol{E} \parallel \boldsymbol{B}$) generate a chiral flow of charge between the two valleys of different chirality[4], with a rate that is proportional to $\boldsymbol{E} \cdot \boldsymbol{B}$. To equilibrate the induced chiral imbalance between the left- and right-handed fermions, large-momentum internode scattering is required, which in general depends on $\boldsymbol{B}$ (refs 11, 27). In the low-field regime, in which many Landau levels are filled, it is possible to solve the corresponding Boltzmann[11] or hydrodynamic[6] transport equation, resulting in a chiral-anomaly-induced positive magneto-conductance contribution of $G = d_e + c_1 a_c^2 B_\parallel^2$. In the high-field limit, in which only the lowest Landau levels contribute to transport, the magneto-conductance

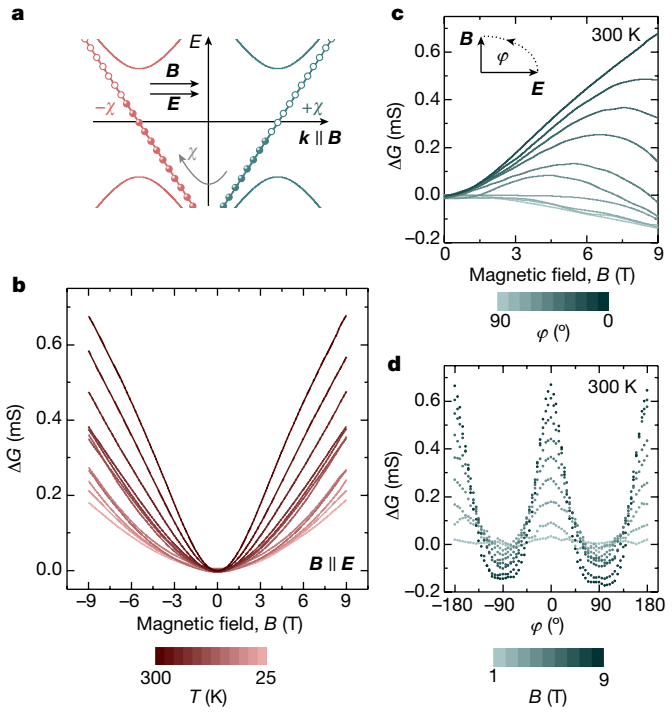

Figure 2 | Chiral anomaly in NbP. a, In a strong magnetic field, the Weyl nodes quantize into Landau levels. The lowest Landau levels exhibit a linear dispersion with distinct chirality ($\pm\chi$). Parallel electric ($\boldsymbol{E}$) and magnetic ($\boldsymbol{B}$) fields pump chiral charges from one cone into the other, which breaks chiral symmetry. **b**, Magneto-conductance without zero-field contributions (ΔG) at selected temperatures (see colour scale), for $\boldsymbol{E} \parallel \boldsymbol{B}$. **c**, ΔG versus $|\boldsymbol{B}|$ for different angles φ (colour scale) between the electric and magnetic fields (see inset), at $T = 300$ K. **d**, Angular dependence of ΔG at $T = 300$ K, for varying magnetic field strength (colour scale).

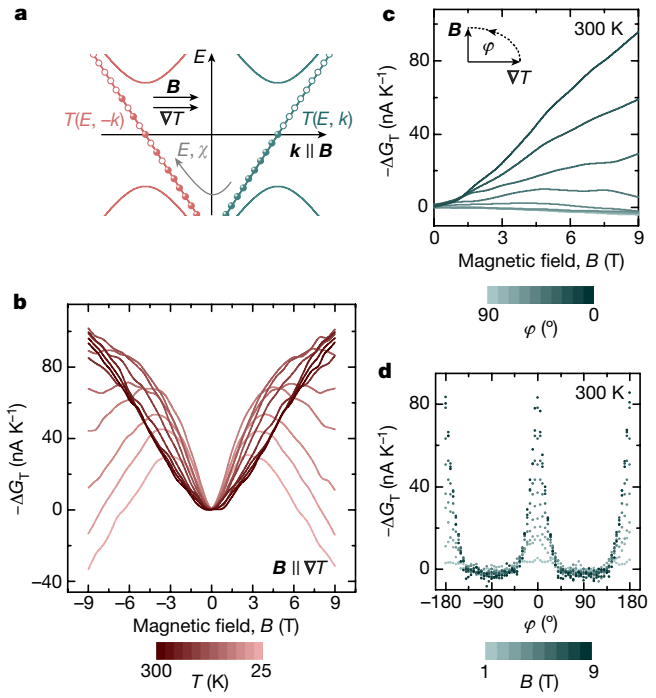

Figure 3 | Evidence of the mixed axial–gravitational anomaly in NbP. a, Parallel temperature gradients (∇T) and magnetic fields ($\boldsymbol{B}$) result in a transfer of particles and energy (E) from one cone to the other. **b**, Negative magneto-thermoelectric conductance without zero-field contributions ($-\Delta G_T$) at selected temperatures (see colour scale), for $\boldsymbol{B} \parallel \nabla T$. The negative sign accounts for electron transport. **c**, $-\Delta G_T$ versus $|\boldsymbol{B}|$ for different angles φ (colour scale) between the temperature gradient and magnetic field (see inset), at $T = 300$ K. The magneto-conductance is negative for $\varphi > 30°$ at high fields. **d**, Angular dependence of $-\Delta G_T$ at $T = 300$ K, for varying magnetic field strength (colour scale).

behaves linearly with applied field. This is the transport fingerprint of the chiral anomaly. As shown in Fig. 2b, we observe a large positive magneto-conductance up to room temperature for $\boldsymbol{E} \parallel \boldsymbol{B}$, which is sensitive to misalignments (Fig. 2c). Whereas the low-field regime is well described by a quadratic fit ($\Delta G \propto B_{\parallel}^2$), in agreement with the Boltzmann description for chiral anomaly, the linear high-field regime can be explained by a transition from a multi-level state to the limit in which only the lowest chiral Landau levels contribute to the transport[14]. Accordingly, with chiral charge pumping, the positive magneto-conductance at low magnetic fields is well approximated by $\cos^2(\varphi)$, where φ is the angle between $\boldsymbol{E}$ and $\boldsymbol{B}$ (Fig. 2d). The narrowing of the angular width at higher fields is caused by strong collimation of the axial beams[12]. The observed locking pattern and the consistent quadratic dependence in the low-field regime are the fundamental signatures of the chiral anomaly[11] and support the description of the system in terms of chiral Weyl fermions.

We now turn to testing the mixed axial–gravitational anomaly in the NbP micro-ribbon. We use a transport experiment, but in this case apply a thermal gradient instead of a voltage bias. Because the NbP sample is short-cut through a near-zero-impedance ammeter, no net electric field is imposed. Excluding electric fields is essential for a clear distinction from the chiral anomaly, which is induced by a finite $\boldsymbol{E} \parallel \boldsymbol{B}$. Instead, applying $\nabla T \parallel \boldsymbol{B}$ leads to a net difference in energy density between the two chiral valley fluids[6,21], proportional to $\nabla T \cdot \boldsymbol{B}$, that is equilibrated through an intervalley energy transfer (Fig. 3a) The resulting imbalance leads to a charge current, owing to the chiral magnetic effect, which then leads to a positive magneto-thermoelectric conductance contribution of $G_T = d_{th} + c_2 a_c a_g B_{\parallel}^2$ (refs 2, 6, 21, 23–26). This phenomenon allows us to probe the presence of the mixed axial–gravitational anomaly through its effect on thermoelectric transport in a condensed matter system. The data corresponding to these measurements are shown in Fig. 3b, c. The applied temperature gradient indeed appears to result in magneto-transport features that are similar to those that result from the application of an electric field. When $\nabla T \parallel \boldsymbol{B}$, the thermoelectrical conductance at low magnetic fields exhibits a positive magneto-thermoelectric conductance that fits to $G_T \propto B_{\parallel}^2$ with the same $\cos^2(\varphi)$ locking pattern as the positive magneto-conductance (Fig. 3d). At high temperatures ($T > 150$ K), the observed dependence of the magneto-transport on the field strength is consistent with the presence of a mixed axial–gravitational anomaly and its corresponding thermoelectric transport prediction[6,23–26]. At lower temperatures, however, we observe a decrease in G_T. This decrease occurs in the same magnetic field range as the crossover from a quadratic to a linear field dependence in ΔG, in agreement with the fact that both effects can be explained by the crossover to a one-dimensional dispersion that Weyl metals show along $\boldsymbol{B}$ in the ultra-quantum limit[15,30]. As we show in Methods, the suppression of thermoelectric transport at high magnetic fields occurs because ΔG_T is proportional to the derivative of the electron density ρ with respect to temperature ($\Delta G_T \propto \partial\rho/\partial T$). Because the density of states is independent of the temperature in the ultra-quantum limit, the electron density at large magnetic fields is independent of temperature and $\Delta G_T = 0$.

The ratio G_T/G should correspond to another measurable transport coefficient, the thermopower S. Starting from the relation $\boldsymbol{J} = G\boldsymbol{E} + G_T \nabla T$, the thermopower S can be determined either from a measurement using an open circuit ($\boldsymbol{J} = \boldsymbol{0}$) or from combining the above experiments at $\boldsymbol{E} = \boldsymbol{0}$ and $\nabla T = \boldsymbol{0}$. The thermopower S expresses the response of the open-circuit voltage to a temperature gradient. To carry out this test, we removed the short-cutting ammeter from our experiment and measured the response of the open-circuit voltage to a temperature gradient in a collinear magnetic field (Fig. 1a). As shown

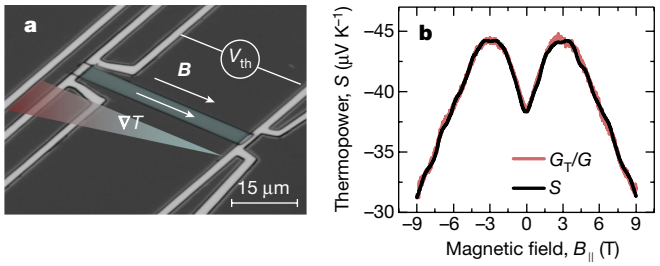

Figure 4 | Longitudinal thermopower. a, False-coloured optical micrograph of the thermopower measurement device. The thermopower $S = V_{th}/|\nabla T|$ is measured along a NbP micro-ribbon (green) by applying a temperature gradient ∇T and measuring the response of the open-circuit voltage V_{th}. **b**, The measured magneto-thermopower S and calculated magneto-thermopower G_T/G of the anomalous transport coefficients match quite well, as demonstrated for $T = 25$ K.

in Fig. 4b, the calculated G_T/G matches the measured S excellently. The agreement is an important cross-check, confirming the results and interpretation above. Furthermore, this result implies that the thermopower is suppressed not solely by the presence of the chiral anomaly, as suggested previously[15], but rather by the presence of both the chiral and mixed axial–gravitational anomalies (Extended Data Fig. 11).

In conclusion, our measurements reveal a positive magneto-thermoelectric conductance in the Weyl semimetal NbP, a signature that is linked to the presence of the mixed axial–gravitational anomaly of chiral fermions in three spatial dimensions. In short, the thermally biased experiment confirms the predicted $B_{\|}^2$ dependence of G_T at low magnetic fields, its dependence on the relative orientation of the magnetic field and the thermal gradient, and the suppression of thermoelectric transport at high magnetic fields. These effects arise concurrently with the standard chiral anomaly, the signatures of which we observed in the field-induced correction to the standard electric conductance. Our results show that it is possible to detect the presence of the mixed axial–gravitational anomaly of Weyl fermions, particularly elusive in other contexts, in relatively simple transport experiments using a macroscopic condensed matter system in a flat space-time.

Online Content Methods, along with any additional Extended Data display items and Source Data, are available in the online version of the paper; references unique to these sections appear only in the online paper.

Received 29 October 2016; accepted 25 May 2017.

1. Bertlmann, R. A. *Anomalies in Quantum Field Theory* (Oxford Univ. Press, 2000).
2. Adler, S. L. Axial-vector vertex in spinor electrodynamics. *Phys. Rev.* **177,** 2426–2438 (1969).
3. Bell, J. S. & Jackiw, R. A PCAC puzzle: $\pi^0 \rightarrow \gamma\gamma$ in the σ-model. *Nuovo Cimento A* **60,** 47–61 (1969).
4. Nielsen, H. B. & Ninomiya, M. The Adler–Bell–Jackiw anomaly and Weyl fermions in a crystal. *Phys. Lett. B* **130,** 389–396 (1983).
5. Landsteiner, K., Megías, E. & Pena-Benitez, F. Gravitational anomaly and transport phenomena. *Phys. Rev. Lett.* **107,** 021601 (2011).
6. Lucas, A., Davison, R. A. & Sachdev, S. Hydrodynamic theory of thermoelectric transport and negative magnetoresistance in Weyl semimetals. *Proc. Natl Acad. Sci. USA* **113,** 9463–9468 (2016).
7. Xu, S.-Y. *et al.* Discovery of a Weyl Fermion semimetal and topological Fermi arcs. *Science* **349,** 613–617 (2015).
8. Xu, S.-Y. *et al.* Discovery of a Weyl fermion state with Fermi arcs in niobium arsenide. *Nat. Phys.* **11,** 748–754 (2015).
9. Huang, S.-M. *et al.* A Weyl fermion semimetal with surface Fermi arcs in the transition metal monopnictide TaAs class. *Nat. Commun.* **6,** 7373 (2015).
10. Nielsen, H. B. & Ninomiya, M. Absence of neutrinos on a lattice: (I). Proof by homotopy theory. *Nucl. Phys. B* **185,** 20–40 (1981).
11. Son, D. T. & Spivak, B. Z. Chiral anomaly and classical negative magnetoresistance of Weyl metals. *Phys. Rev. B* **88,** 104412 (2013).
12. Xiong, J. *et al.* Evidence for the chiral anomaly in the Dirac semimetal Na_3Bi. *Science* **350,** 413–416 (2015).
13. Huang, X. *et al.* Observation of the chiral-anomaly-induced negative magnetoresistance in 3D Weyl semimetal TaAs. *Phys. Rev. X* **5,** 031023 (2015).
14. Niemann, A. C. *et al.* Chiral magnetoresistance in the Weyl semimetal NbP. *Sci. Rep.* **7,** 43394 (2017).
15. Hirschberger, M. *et al.* The chiral anomaly and thermopower of Weyl fermions in the half-Heusler GdPtBi. *Nat. Mater.* **15,** 1161–1165 (2016).
16. Li, H. *et al.* Negative magnetoresistance in Dirac semimetal Cd_3As_2. *Nat. Commun.* **7,** 10301 (2016).
17. Arnold, F. *et al.* Negative magnetoresistance without well-defined chirality in the Weyl semimetal TaP. *Nat. Commun.* **7,** 11615 (2016).
18. Shekhar, C. *et al.* Observation of chiral magneto-transport in RPtBi topological Heusler compounds. Preprint at https://arxiv.org/abs/1604.01641 (2016).
19. Alvarez-Gaumé, L. & Witten, E. Gravitational anomalies. *Nucl. Phys. B* **234,** 269–330 (1984).
20. Eguchi, T. & Freund, P. G. O. Quantum gravity and world topology. *Phys. Rev. Lett.* **37,** 1251–1254 (1976).
21. Landsteiner, K., Megías, E. & Peña-Benitez, F. in *Strongly Interacting Matter in Magnetic Fields* (eds Kharzeev, D. *et al.*) 433–468 (Springer, 2013).
22. Kaminski, M., Uhlemann, C. F., Bleicher, M. & Schaffner-Bielich, J. Anomalous hydrodynamics kicks neutron stars. *Phys. Lett. B* **760,** 170–174 (2016).
23. Lundgren, R., Laurell, P. & Fiete, G. A. Thermoelectric properties of Weyl and Dirac semimetals. *Phys. Rev. B* **90,** 165115 (2014).
24. Kim, K.-S. Role of axion electrodynamics in a Weyl metal: violation of Wiedemann–Franz law. *Phys. Rev. B* **90,** 121108(R) (2014).
25. Sharma, G., Goswami, P. & Tewari, S. Nernst and magnetothermal conductivity in a lattice model of Weyl fermions. *Phys. Rev. B* **93,** 035116 (2016).
26. Spivak, B. Z. & Andreev, A. V. Magnetotransport phenomena related to the chiral anomaly in Weyl semimetals. *Phys. Rev. B* **93,** 085107 (2016).
27. Burkov, A. A. Chiral anomaly and diffusive magnetotransport in Weyl metals. *Phys. Rev. Lett.* **113,** 247203 (2014).
28. Shekhar, C. *et al.* Extremely large magnetoresistance and ultrahigh mobility in the topological Weyl semimetal candidate NbP. *Nat. Phys.* **11,** 645–649 (2015).
29. Sergelius, P. Berry phase and band structure analysis of the Weyl semimetal NbP. *Sci. Rep.* **6,** 33859 (2016).
30. Liang, T. *et al.* Evidence for massive bulk Dirac fermions in $Pb_{1-x}Sn_xSe$ from Nernst and thermopower experiments. *Nat. Commun.* **4,** 2696 (2013).

Acknowledgements This work was supported by the research grant DFG-RSF (NI616 22/1) 'Contribution of topological states to the thermoelectric properties of Weyl semimetals', Severo Ochoa SEV-2012-0249, FPA 2015-65480-P and SFB 1143, by the Helmholtz association through VI-521, and by the DFG (Emmy Noether programme) via grant ME 4844/1. We thank T. Sturm and A. Pöhl, for experimental support. We also acknowledge support by W. Riess, K. Moselund and H. Riel, and thank C. Bollinger for copy-editing.

Author Contributions J.G. conceived the experiment. M.S., C.S. and V.S. synthesized the single-crystal bulk samples. R.H. characterized the crystal structure. B.R. supervised the micro-ribbon definition and the compositional analysis. A.C.N. fabricated the samples. J.G. carried out the thermoelectric transport measurements with the help of A.C.N. J.G., A.C.N., F.M., B.G., T.M. and A.G.G. analysed the data. B.G., C.F., B.Y. and K.N. supervised the project. A.G.G., T.M. and K.L. provided the theoretical background for the work. All authors contributed to interpreting the data and writing the manuscript.

Author Information Reprints and permissions information is available at www.nature.com/reprints. The authors declare no competing financial interests. Readers are welcome to comment on the online version of the paper. Publisher's note: Springer Nature remains neutral with regard to jurisdictional claims in published maps and institutional affiliations. Correspondence and requests for materials should be addressed to J.G. (Johannes.gooth@outlook.com).

METHODS

Micro-ribbon fabrication. High-quality single bulk crystals of NbP are grown via a chemical vapour transport reaction using an iodine transport agent. A polycrystalline powder of NbP is synthesized by direct reaction of niobium (Chempur 99.9%) and red phosphorus (Heraeus 99.999%) within an evacuated fused silica tube for 48 h at 800 °C. The growth of bulk single crystals of NbP is then initialized from this powder by chemical vapour transport in a temperature gradient, starting from 850 °C (source) and increasing to 950 °C (sink), and in a transport agent with a concentration of 13.5 mg cm^{-3} iodine (Alfa Aesar 99.998%).

Subsequently, NbP micro-ribbons are cut out from the bulk crystals (Extended Data Fig. 1a,b) using gallium focused-ion beam etching (voltage, 30 kV; current, 65–80 pA). The samples are prepared such that their longitudinal direction coincides with the [100] crystal axis of NbP. Focused-ion beam etching caused *in situ* gallium doping of the ribbons. The final composition of the samples is analysed by scanning electron microscopy energy-dispersive X-ray spectroscopy (SEM-EDX), yielding 53% Nb, 45% P and 2% Ga (Extended Data Fig. 1c). We study ribbons 50 μm × 2.5 μm × 0.5 μm in size. The dimensions of the ribbons are obtained from SEM. The high aspect ratio of our samples ensures the suppression of jet currents during the transport measurements. The single-crystallinity of the ribbons is evident from the X-ray diffraction (XRD) pattern shown in Extended Data Fig. 1d.

Device fabrication. After cutting, the NbP micro-ribbons are directly transferred onto Si/SiO_2 chips in a solvent-less approach, using a micromanipulator. A soft mask for electrical contacts to the micro-ribbon is defined via laser-beam lithography (customized μPG system). A double layer of photoresist is spin-coated and baked (first photoresist: LOR 3B, spin-coated at 3,500 r.p.m. for 45 s, baked at 180 °C for 250 s; second photoresist: ma-P 1205, spin-coated at 3,500 r.p.m. for 30 s, baked at 100 °C for 30 s), before laser exposure and development for 40 s in ma-D 331 solution. Sputter deposition of Ti/Pt (10 nm/400 nm) is performed after 5 min of argon sputter cleaning. Titanium serves as the adhesion promoter and diffusion barrier for the platinum. Finally, a lift-off is performed, 1 h at 80 °C in Remover 1165. An optical micrograph of a final device is shown in Extended Data Fig. 2.

Thermoelectric measurements. Thermoelectric measurements are performed in a temperature-variable cryostat (Dynacool, Quantum Design) in vacuum. The cryostat is equipped with a ±9 T superconducting magnet. After fabrication, the micro-ribbon devices are wire bonded and mounted on a sample holder that allows rotation in angles from −10° to 370°. We specifically investigate three thermoelectric transport parameters of the NbP micro-ribbons: the electrical conductance $G = J/V$, the thermoelectric conductance $G_T = J/|\nabla T|$, and the thermopower $S = -V_{th}/|\nabla T|$, where J denotes the electrical current, V the voltage bias, ∇T a temperature gradient and V_{th} the voltage response to ∇T. All transport coefficients are measured in the linear response regime as a function of the cryostat base temperature T, magnetic field $\boldsymbol{B}$ and rotation angle φ, which is defined with respect to the transport direction along the longitudinal axis of the samples.

Electrical conductance measurements in a two-probe configuration are carried out under isothermal conditions with d.c. bias voltages of up to $V = 1$ mV applied with a Yokogawa voltage source and a 100-times voltage divider across the length of the ribbon. Our results are independent of contact iteration. The responding current signal J is enhanced using a current preamplifier (Stanford Research, model SR570) with an input impedance of 1 Ω. Contact lines across the full width of the sample ensure a homogeneous electric field distribution in the ribbon. Temperature-dependent J–V measurements (Extended Data Fig. 3) reveal ohmic contacts. The magneto-conductance is measured by sweeping the magnetic field with 5 mT s^{-1}.

Thermoelectric conductance measurements are performed with the same current recording set-up, but, crucially, without an electric field imposed at the sample. Instead, the on-chip Joule heater line near the end of the micro-ribbon is used to generate a temperature gradient ∇T along the length of the micro-ribbon. ∇T is measured by resistive thermometry, using two metal four-probe thermometer lines located at the ends of the micro-ribbons (Extended Data Fig. 2). The thermometers are driven by lock-in amplifiers (Stanford Research, model SR830) with a 500-nA a.c. bias current at distinct frequencies (<15 Hz) to prevent crosstalk. The thermometers are calibrated under isothermal conditions against the base temperature of the cryostat (Extended Data Fig. 4), from which $T(R)$ is determined, where R is the electrical resistance of the thermometers. The heating voltage V_H applied across a 2-kΩ shunt resistance at the heater line (Extended Data Fig. 5) is chosen to ensure a linear response of the current J to the temperature gradient ($J \propto |\nabla T|$; Extended Data Fig. 6). G_T is then obtained from linear fits of J versus the corresponding $|\nabla T|$ at fixed base temperatures; $|\nabla T|$ values of up to 350 mK are obtained. The magneto-thermoelectric conductance is measured at a fixed heating voltage of 12 V, sweeping the magnetic field with 5 mT s^{-1}. ∇T showed no dependence on the magnetic field. The field sweeping rate is chosen such that the results are independent of it.

To obtain S, the current measurement set-up is removed and replaced by a nanovoltmeter (Keithley, model 182A) to measure the open-circuit voltage V_{th} of the NbP micro-ribbons in response to ∇T. Choosing the same V_H as in the thermoelectric conductance measurements ensures a linear response of V_{th} to the temperature gradient ($V_{th} \propto |\nabla T|$; Extended Data Fig. 7). S is then extracted from linear fits of V_{th} versus $|\nabla T|$.

Temperature dependence of the transport coefficients at zero magnetic field. In the absence of an applied magnetic field, the electrical conductance exhibits a non-metallic $G(T)$ dependence with a negative temperature coefficient of resistance (Extended Data Fig. 8). Furthermore, without magnetic and electric fields applied along the sample, the measurement of thermoelectric conductance versus temperature reveal a change in sign at approximately 250 K (Extended Data Fig. 9). Below 250 K, the transport in the NbP micro-ribbons is dominated by conduction-band electrons, indicated by a negative sign of the thermoelectric conductance in the G_T–T plot. Because of the zero bandgap, holes are thermally excited in parallel, governing the transport at higher temperatures (positive G_T). The same generic features are observed in $S(T)$ (Extended Data Fig. 10).

Connection between the mixed axial–gravitational anomaly and thermal transport. *The mixed axial–gravitational anomaly.* For completeness, we present established quantum field theory and hydrodynamic theory results for chiral Weyl fermions that support the interpretation that the measurements presented here stem from a mixed axial–gravitational anomaly. We start by noting that, unlike pure gravitational anomalies, which are allowed only in space-time dimension $D = 4k - 2$, where k is an integer, mixed axial–gravitational anomalies are allowed in the $D = 3 + 1$ that is relevant for Weyl semimetals[19]. In particular, we are interested in the Abelian version of the mixed axial–gravitational anomaly, which is expressed via the non-conservation of axial current j^μ_A in a curved space-time that is characterized by the Riemann tensor $R^\alpha_{\beta\mu\nu}$. Following the notation of ref. 21, we write the conservation law for this current as

$$\partial_\mu j^\mu_A = \frac{d_{AVV}}{32\pi^2}\varepsilon^{\mu\nu\rho\sigma}F^V_{\mu\nu}F^V_{\rho\sigma} + \frac{b_A}{768\pi^2}\varepsilon^{\mu\nu\rho\sigma}R^\alpha_{\beta\mu\nu}R^\beta_{\alpha\rho\sigma} \quad (1)$$

where the labels 'A' and 'V' denote tensors built out of axial and vector fields, respectively, and d_{AVV} and b_A are numerical coefficients (defined below). The first term on the right-hand side of equation (1) represents the non-conservation of axial current due to the presence of external non-orthogonal electric and magnetic fields. It involves the electromagnetic (vector) field strength $F^V_{\mu\nu} = \partial_\mu A^V_\nu - \partial_\nu A^V_\mu$ through the U(1) vector gauge field A^V_ν where $\mu \in \{0, 1, 2, 3\}$. Its coefficient is set by the chiral anomaly coefficient d_{abc}, with $a, b, c \in \{A, V\}$; when $d_{abc} \neq 0$, the chiral anomaly is present. For the Abelian case, of interest here, it is simply determined by the difference between a triple product of charges q of right ('r') and left ('l') chirality:

$$d_{abc} = \sum_r \left(q^r_a q^r_b q^r_c\right) - \sum_l \left(q^l_a q^l_b q^l_c\right)$$

where $q^r_V = q^r_A = 1$ and $q^l_V = -q^l_A = 1$. Therefore, $d_{AVV} = 2$ for a pair of chiral fermions.

The second term on the right-hand side of equation (1) is the contribution of the mixed axial–gravitational anomaly to the non-conservation of chiral current. In the Abelian case, its coefficient is given by

$$b_a = \sum_r q^r_a - \sum_l q^l_a$$

with $a \in \{A, V\}$. If $b_a \neq 0$, then the mixed axial–gravitational anomaly is present[1,3,4] and $b_a = 2$ for each pair of chiral fermions.

Connection with thermal transport. Given the form of the gravitational term in equation (1), it is natural to ask how it is possible to detect its presence in a flat space-time in which $R^\alpha_{\beta\mu\nu} = 0$. The key but subtle observation is that the temperature dependence of linear transport coefficients for systems of Weyl fermions depends on a_g, even in flat space-time. This conclusion can be reached from the standard Kubo formalism[5], holography[31], hydrodynamic theory[8] or arguments based on a global version of the axial–gravitational anomaly[32].

Although hydrodynamic[6] and Kubo approaches lead to consistent predictions for the thermoelectric coefficient presented here, the former relies on interactions being the dominant scattering mechanism. Because the scattering in experimental samples seems to be mostly dominated by impurity scattering, we believe the Kubo approach to be more suitable for the description of our data.

In what follows we sketch a simple derivation that justifies the functional form of the positive magneto-thermoelectric conductance that we use. We consider a single Weyl cone, in which case the anomaly coefficients are $d_\chi = b_\chi = \pm 1$, and we define $a_\chi = d_\chi/(4\pi^2)$ and $a_g = b_\chi/24$. Our calculation relies on the Kubo formalism; although the low-field predictions obtained by this treatment are consistent with those from Boltzmann kinetic theory[23–26], key advantages of the Kubo formalism as compared to the Boltzmann approach are that it tracks the relationship to the

mixed axial–gravitational anomaly in a transparent way and that it is directly applicable to large magnetic fields. We start with the equations that describe particle and energy conservation for a single Weyl fermion:

$$\dot{\rho} + \boldsymbol{\nabla} \boldsymbol{J}_\rho = a_\chi \boldsymbol{E} \cdot \boldsymbol{B} \tag{2}$$

$$\dot{\epsilon} + \boldsymbol{\nabla} \boldsymbol{J}_\epsilon = \boldsymbol{J}_\rho \cdot \boldsymbol{E} \tag{3}$$

where ρ is the electronic density and ϵ is the energy density. $\boldsymbol{J}_\rho$ and $\boldsymbol{J}_\epsilon$ are the electric and the energy current, respectively. Because the system lives in flat space-time, only the chiral anomaly enters these equations. We furthermore note that the energy conservation equation (3) includes a term that describes the work performed by the electric field.

We are interested in the magnetic-field-dependent contribution to the energy and charge current that will ultimately determine the positive magneto-thermoelectric conductance. As discussed in ref. 20, the standard Kubo formalism for Weyl fermions leads to

$$\boldsymbol{J}_\rho = a_\chi \mu \boldsymbol{B} \tag{4}$$

$$\boldsymbol{J}_\epsilon = \left(\frac{a_\chi}{2} \mu^2 + a_g T^2 \right) \boldsymbol{B} \tag{5}$$

Equation (4) describes the chiral magnetic effect for a single Weyl fermion at chemical potential μ, which depends on the chiral anomaly coefficient a_χ. The energy current given in equation (5) is composed of two terms. The first term describes that the directed flow of particles in a system with a chiral anomaly leads to an energy current that is simply due to the energy associated with each electronic state. This term is normalized such that the energy current vanishes in the vacuum state, which corresponds to $\mu = 0$. The second term, which describes the thermal contribution of interest, has recently been highlighted to be a consequence of the mixed axial–gravitational anomaly[5,31–35]. It is hence governed by the coefficient a_g, which establishes a link between the existence of a thermal contribution in $\boldsymbol{J}_\epsilon$ and the gravitational contribution to equation (1).

We now turn to the thermoelectric transport. To this end, we assume a finite magnetic field $\boldsymbol{B}$ and compute the anomalous response due to a gradient in temperature $\boldsymbol{\nabla} T$ and an electric field $\boldsymbol{E}$ (all of which are assumed to be spatially homogeneous) in the linear-response approximation. With these assumptions, we can insert equations (4) and (5) into equations (2) and (3) to obtain

$$\dot{\epsilon} = a_\chi \mu \boldsymbol{E} \cdot \boldsymbol{B} - 2 a_g T \boldsymbol{\nabla} T \cdot \boldsymbol{B} \tag{6}$$

$$\dot{\rho} = a_\chi \boldsymbol{E} \cdot \boldsymbol{B} \tag{7}$$

The first term on the right-hand side of (6) is the work performed by the electric field on the background chiral-magnetic-effect current. If there are two nodes of opposite chirality, then this term encodes that each particle pumped between the Weyl nodes in parallel electric and magnetic fields also transfers its energy from one node to the other. The second term on the right-hand side of equation (6) shows that, in a completely analogous way, a temperature gradient parallel to the magnetic field leads to energy pumping between Weyl cones owing to the mixed axial–gravitational anomaly. In a Weyl semimetal, intervalley scattering will stop this pumping on a timescale τ, known as the intervalley scattering time. (In a strongly interacting electron fluid the energies of different Weyl cones could in principle equilibrate on a shorter timescale, owing to electron–electron interactions; however, this is not the case here.) The steady state is accounted for by the replacement $(\dot{\epsilon}, \dot{\rho}) \to (\delta\epsilon, \delta\rho)/\tau$.

At this point it is convenient to introduce the matrix

$$\Xi = \begin{pmatrix} \dfrac{\partial \epsilon}{\partial T} & \dfrac{\partial \epsilon}{\partial \mu} \\ \dfrac{\partial \rho}{\partial T} & \dfrac{\partial \rho}{\partial \mu} \end{pmatrix}$$

such that

$$\begin{pmatrix} \delta\epsilon \\ \delta\rho \end{pmatrix} = \Xi \begin{pmatrix} \delta T \\ \delta\mu \end{pmatrix}$$

and equations (6) and (7) can be written as

$$\Xi \begin{pmatrix} \delta T \\ \delta\mu \end{pmatrix} = \tau \begin{pmatrix} -2 a_g T & a_\chi \mu \\ 0 & a_\chi \end{pmatrix} \begin{pmatrix} \boldsymbol{\nabla} T \\ \boldsymbol{E} \end{pmatrix} \boldsymbol{B} \tag{8}$$

From equations (4) and (5), we obtain the ith components of the energy and particle currents,

$$\begin{pmatrix} \delta J_{\epsilon,i} \\ \delta J_{\rho,i} \end{pmatrix} = \tau \begin{pmatrix} 2 a_g T & a_\chi \mu \\ 0 & a_\chi \end{pmatrix} \begin{pmatrix} \delta T \\ \delta\mu \end{pmatrix} B_i$$

which together with equation (8) define the response tensor κ_{ij} as

$$\kappa_{ij} = \begin{pmatrix} 2 a_g T & a_\chi \mu \\ 0 & a_\chi \end{pmatrix} \Xi^{-1} \begin{pmatrix} -2 a_g T & a_\chi \mu \\ 0 & a_\chi \end{pmatrix} \tau B_i B_j$$

The anomaly-induced response in the current is thus given by

$$J_i = G_T^{ij} \nabla_j T + G^{ij} E_j$$

where the conductance tensors have components

$$G^{ij} = \tau \frac{a_\chi^2}{\det(\Xi)} \left(\frac{\partial \epsilon}{\partial T} - \mu \frac{\partial \rho}{\partial T} \right) B_i B_j \tag{9}$$

$$G_T^{ij} = \tau \frac{2 a_\chi a_g T}{\det(\Xi)} \frac{\partial \rho}{\partial T} B_i B_j \tag{10}$$

To explain our experimental measurements, we now consider the regimes of either low or high magnetic field, assuming a homogenous Fermi velocity of v_F (we use units such that the elementary charge $e = 1$). In the first case, the system behaves as a gas of free Weyl fermions with an energy density of

$$\epsilon = \frac{1}{8\pi^2 v_F^3} \left(\mu^4 + 2\pi^2 T^2 \mu^2 + \frac{7}{15} \pi^4 T^4 \right) \tag{11}$$

(see for instance ref. 36). In the second case, the system splits into degenerate one-dimensional systems, the number of which is set by the Landau level degeneracy, and the energy density is

$$\epsilon_B = \frac{|\boldsymbol{B}|}{v_F} \left(\frac{\mu^2}{8\pi^2} + \frac{T^2}{24} \right) \tag{12}$$

For small and large magnetic fields, the particle densities are given respectively by

$$\rho = \frac{\mu^3 + \pi^2 T^2 \mu}{6\pi^2 v_F^3} \tag{13}$$

and

$$\rho_B = \frac{|\boldsymbol{B}|}{4\pi^2 v_F} \mu \tag{14}$$

Combining the above allows us to obtain G^{ij} and G_T^{ij} in different magnetic-field regimes. For low magnetic fields, substituting equations (11) and (13) into equation (9) yields

$$G^{ij} = \frac{6 a_\chi^2 \pi^2 v_F^3 (7\pi^2 T^2 + 5\mu^2)}{7\pi^4 T^4 + 6\mu^2 T^2 \mu^2 + 15\mu^4} \tau B_i B_j \tag{15}$$

$$G_T^{ij} = \frac{120 a_\chi a_g \pi^2 T \mu v_F^3}{7\pi^4 T^4 + 6\mu^2 T^2 \mu^2 + 15\mu^4} \tau B_i B_j \tag{16}$$

whereas, for large magnetic fields, substituting equations (12) and (14) into equation (9) leads to

$$G^{ij} = 4 a_\chi^2 \pi^2 v_F \tau \frac{B_i B_j}{|\boldsymbol{B}|}$$

$$G_T^{ij} = 0$$

By adding a Drude contribution and summing over the contributions from the different nodes, we obtain the functional form used in the main text.

Equations (10) and (16) establish a link between the presence of the chiral and mixed axial–gravitational anomalies, represented by $a_\chi \neq 0$ and $a_g \neq 0$, respectively, and the enhancement of the thermoelectric response function of Weyl fermions in flat space-time due to a magnetic field applied parallel to a thermal gradient.

In particular, if the axial–gravitational anomaly is absent, then there is no thermal transport. Because we probe the presence of the chiral anomaly ($a_\chi \neq 0$) independently by measuring a positive magneto-conductance, our results indicate that $a_g \neq 0$. This is the main finding of our work.

The physical effects can be summarized as follows. The thermal gradient increases (decreases) the energy density of left-moving (right-moving) charge carriers, which leads to an effective chiral imbalance that generates a current in the direction of the magnetic field via the chiral magnetic effect. Finally, as mentioned above and in the main text, the functional dependence used in here is consistent with more conventional semi-classical treatments based on the Boltzmann equation[23–26]; however, these do not track the origin of these anomalous transport features explicitly, and cannot access the high-magnetic-field limit directly.

Data availability. All data generated and analysed during this study are available within the paper and its Extended Data. Further data are available from the corresponding author on reasonable request.

31. Landsteiner, K., Megias, E., Melgar, L. & Pena-Benitez, F. Holographic gravitational anomaly and chiral vortical effect. *J. High Energy Phys.* **9,** 121 (2011).
32. Golkar, S. & Sethi, S. Global anomalies and effective field theory. *J. High Energy Phys.* **5,** 105 (2016).
33. Delbourgo, R. & Salam, A. The gravitational correction to PCAC. *Phys. Lett. B* **40,** 381–382 (1972).
34. Landsteiner, K. Notes on anomaly induced transport. *Acta Phys. Pol. B* **47,** 2617–2673 (2016).
35. Jensen, K., Loganayagam, R. & Yarom, A. Thermodynamics, gravitational anomalies and cones. *J. High Energy Phys.* **2,** 88 (2013).
36. LeBellac, M. *Thermal Field Theory* (Cambridge Univ. Press, 2000).

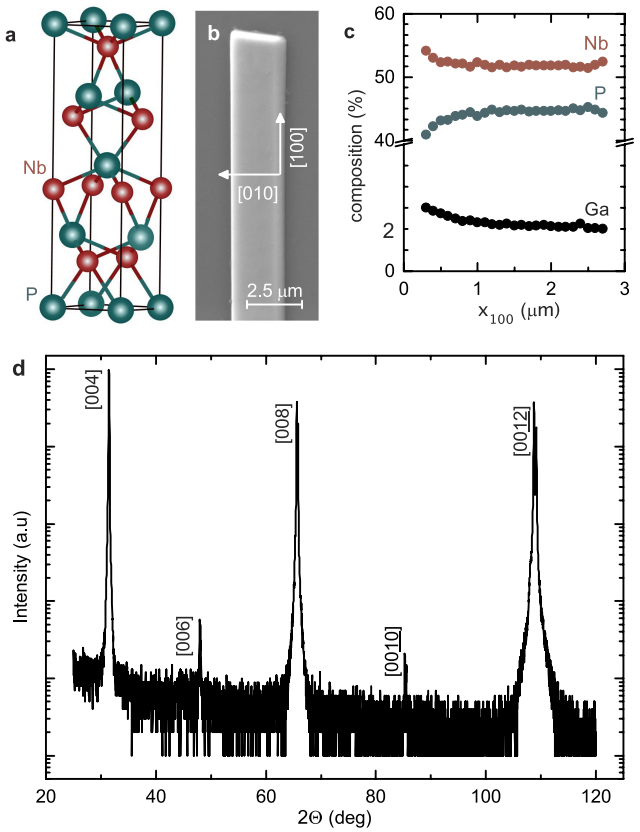

Extended Data Figure 1 | Material analysis of the NbP micro-ribbon. **a**, Sketch of the structure of the NbP crystal. **b**, SEM image of a NbP micro-ribbon before device processing. The longitudinal direction of the ribbon corresponds to the [100] axis of the crystal. **c**, Spatial composition of an exemplary NbP micro-ribbon, measured from the top along [100] using SEM-EDX, reveals an average of 53% Nb, 45% P and 2% Ga. x_{100} is the distance from the end of the sample along [100]. **d**, XRD spectrum of the NbP at room temperature (Cu K_α radiation). a.u., arbitrary units.

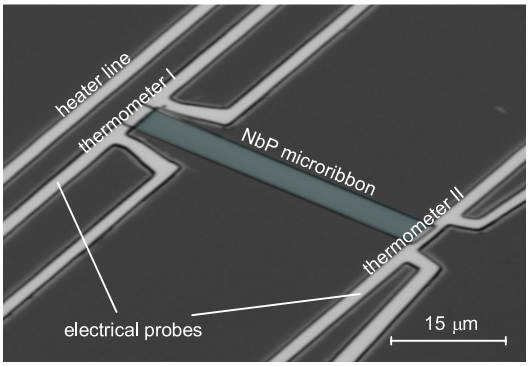

Extended Data Figure 2 | Optical micrograph of a measurement device. The NbP micro-ribbon (green) is placed between two four-probe thermometers (grey), which also serve as electrical probes. The electrically insulated heater line (grey) close to one end of the sample creates a temperature gradient along the length of the sample.

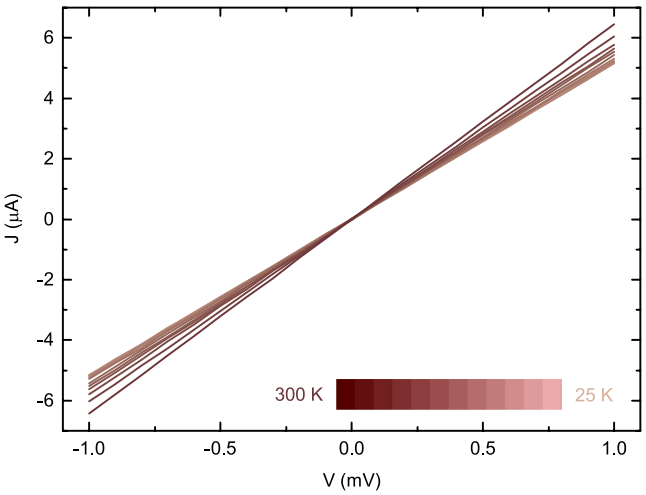

Extended Data Figure 3 | Isothermal ($\nabla T = 0$ K) current–voltage ($J-V$) characteristic of the NbP micro-ribbon at selected temperatures and zero magnetic field ($B = 0$ T). The linearity of the curves reveals ohmic electrical contacts.

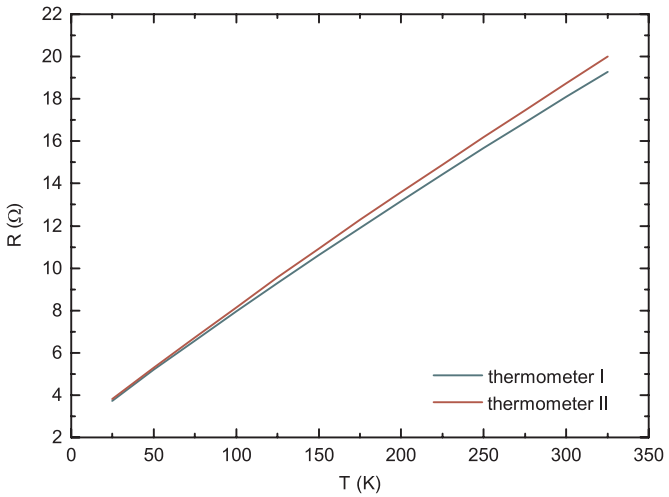

Extended Data Figure 4 | Thermometer calibration. Resistance *R* versus base temperature *T* of the cryostat, measured at isothermal conditions.

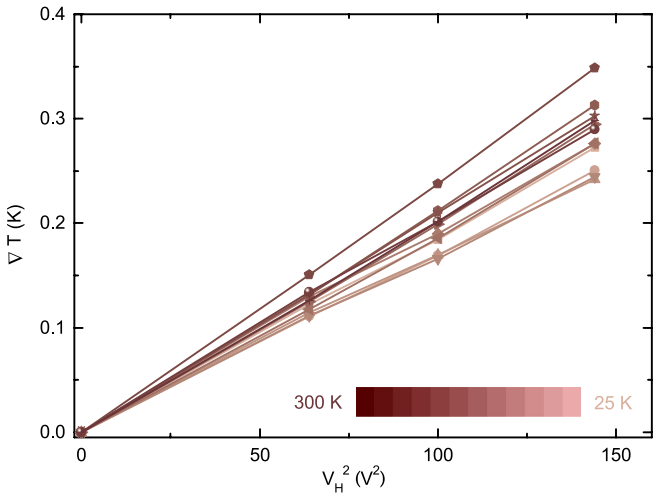

Extended Data Figure 5 | Temperature gradient ∇T along the sample as a function of the square of the heating voltage V_H at different base temperatures, which is proportional to the heating power.

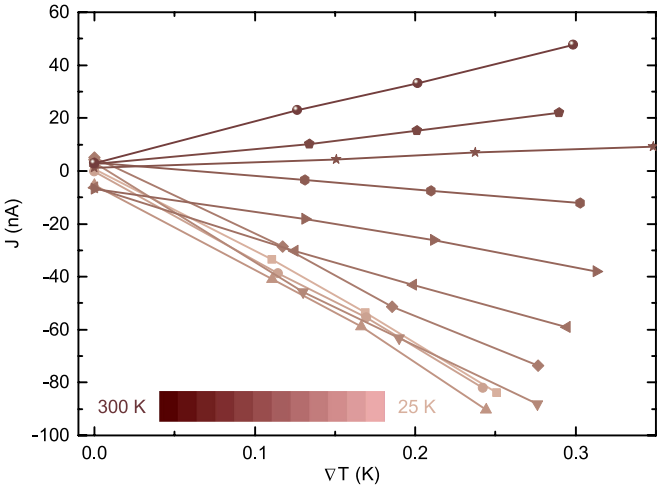

Extended Data Figure 6 | Linear response of the thermoelectric current *J* to the temperature gradient ∇T. We determine the thermoconductance $G_T = J/|\nabla T|$ from the slope of the linear fits. The error bars in Extended Data Fig. 8b are the uncertainties obtained from these fits.

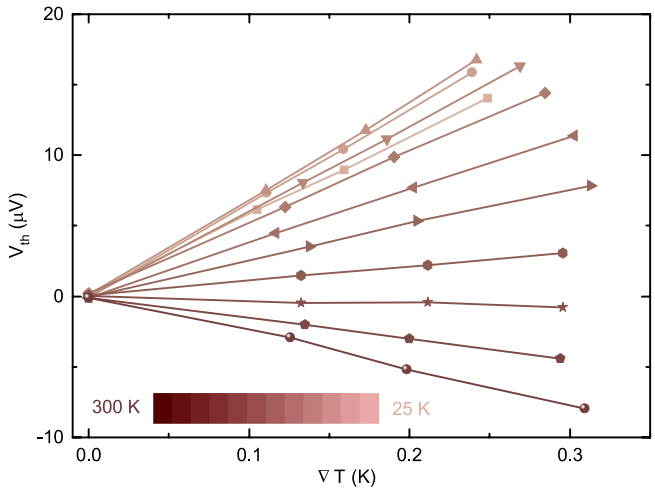

Extended Data Figure 7 | Linear response of the thermovoltage V_{th} to the temperature gradient ∇T. The thermopower $S = -V_{th}/|\nabla T|$ is determined from linear fits of the data.

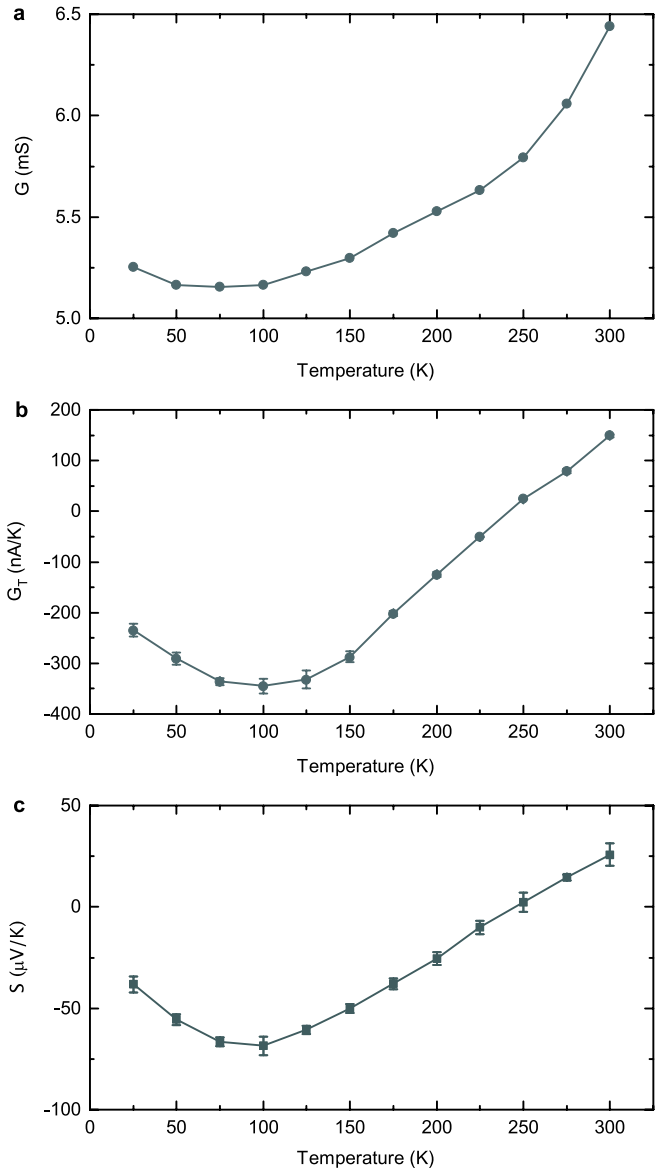

Extended Data Figure 8 | Zero-field transport. a, Electrical conductance G at zero magnetic field ($\boldsymbol{B}=\mathbf{0}$ T) in isothermal conditions ($\boldsymbol{\nabla} T=\mathbf{0}$ K) as a function of the base temperature. Values of G are obtained from the slope of the linear fits of the data given in Extended Data Fig. 3. **b**, Thermoelectric conductance G_T at zero magnetic field ($\boldsymbol{B}=\mathbf{0}$ T) and with no electric field imposed ($\boldsymbol{E}=\mathbf{0}$) as a function of the base temperature. Values of G_T are obtained from the slope of the linear fits of the data shown in Extended Data Fig. 6. Error bars, fit uncertainty of the slope. **c**, Themopower S at zero magnetic field ($\boldsymbol{B}=\mathbf{0}$ T) as a function of the base temperature. Values of S are obtained from the slope of the linear fits of the data shown in Extended Data Fig. 7. Error bars, fit uncertainty of the slope.

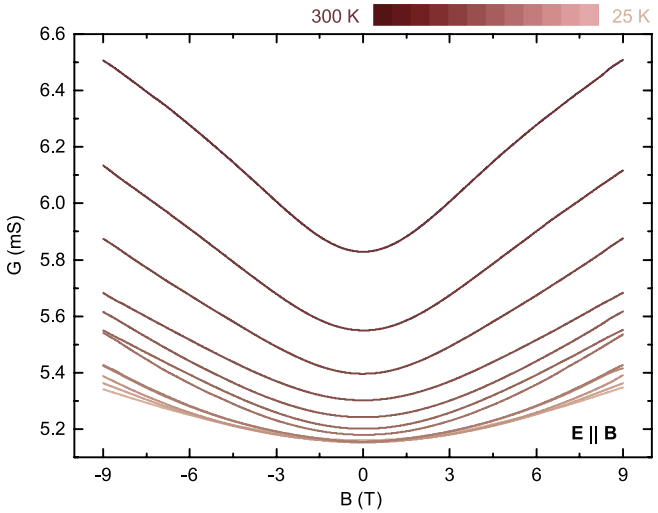

Extended Data Figure 9 | Magneto-conductance $G(E \parallel B)$ as a function of magnetic field B at selected base temperatures (colour scale).

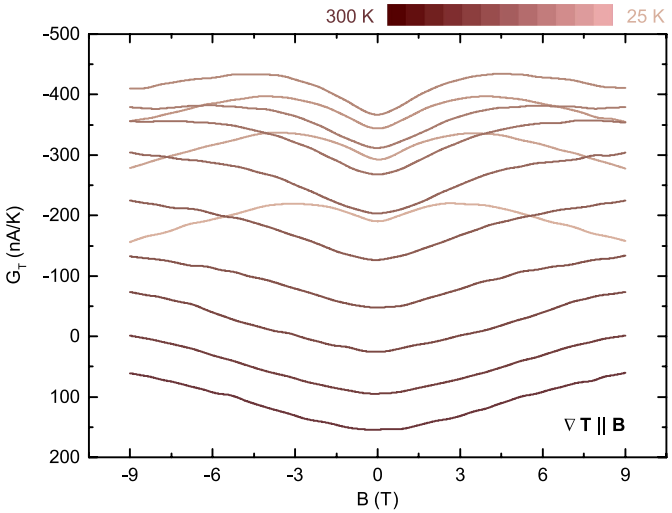

Extended Data Figure 10 | Magneto-thermoelectric conductance $G_T(\nabla T \parallel B)$ as a function of magnetic field B at selected base temperatures (colour scale).

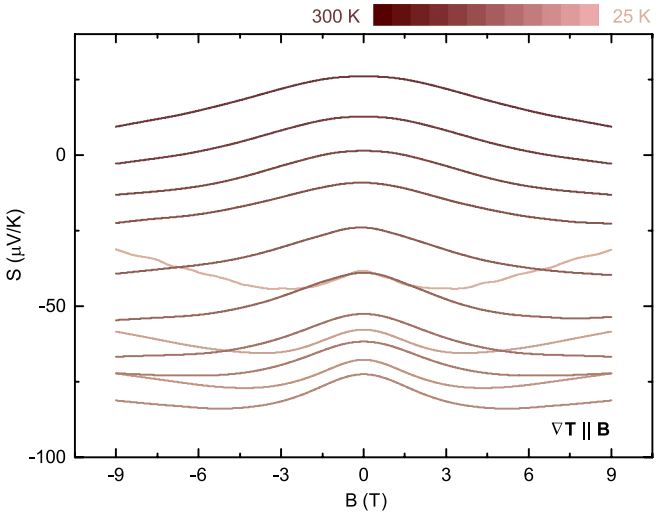

Extended Data Figure 11 | Magneto-thermopower $S(\nabla T \parallel B)$ as a function of magnetic field B at selected base temperatures (colour scale).